Journal of Power Sources 195 (2010) 2310–2318

Contents lists available at ScienceDirect

Journal of Power Sources

journal homepage: www.elsevier.com/locate/jpowsour

Modeling of thermal stresses and lifetime prediction of planar solid oxide fuel cell under thermal cycling conditions

Lin Liu, Gap-Yong Kim*, Abhijit Chandra

Department of Mechanical Engineering, Iowa State University, Ames, IA 50011, USA

ARTICLE INFO

Article history:
Received 29 July 2009
Received in revised form 15 October 2009
Accepted 16 October 2009
Available online 30 October 2009

Keywords:
SOFC
Modeling
Thermal cycling
Thermal stress
Failure
Degradation

ABSTRACT

A typical operating temperature of a solid oxide fuel cell (SOFC) is above 600 °C, which leads to severe thermal stresses caused by the difference in material mechanical properties during thermal cycling. Interfacial shear stress and peeling stress are the two types of thermal stresses that can cause the mechanical failure of the SOFC. Two commonly used SOFC configurations (electrolyte-supported and anode-supported) were considered for this study. The paper developed a mathematical model to estimate the thermal stresses and to predict the lifetime of the cell (Ni/8YSZ–YSZ–LSM). Due to the mismatch of the material mechanical properties of the cell layers, a crack nucleation induced by thermal stresses can be predicted by the crack damage growth rate and the initial damage distribution in the interfacial layer for each thermal cycle. It was found that the interfacial shear stress and peeling stress were more concentrated near the electrode free edge areas. The number of cycles needed for failure decreased with the increase in the porosity of electrode. The number of cycle for failure decreased with increase in electrolyte thickness for both anode- and electrolyte-supported SOFC. The model provides insight into the distribution of interfacial shear stress and peeling stress and can also predict damage evolution in a localized damage area in different SOFC configurations.

1. Introduction

Degradation of a solid oxide fuel cell (SOFC) is often referred to as the decrease of a cell's electrical performance or mechanical failure [1–4]. The consequences of thermal stress and redox cycle where the nickel anode is repeatedly oxidized and reduced lead to performance degradation and shortening of the SOFC lifetime [5]. It has been reported that the decrease of the overall cell electrical performance is mainly due to the degradation of the anode microstructure [6–9]. For the Ni anode SOFC, there are three anode degradation mechanisms [1]: (1) material transport mechanism; (2) thermomechanical mechanism; and (3) deactivation and passivation mechanism. There have been reports and observations of catastrophic mechanical failure of SOFCs during thermal cycling [4,10–13]. As the operating temperature of a SOFC is typically above 600 °C, thermomechanical mechanism is likely the cause of such abrupt failure. Severe thermal stress induced by different material mechanical properties during the thermal cycling can make the interface layers to delaminate.

The two main failure modes of a SOFC, delamination and transgranular fracture, have been observed by several researchers. Cai et al. [14] investigated the constrained densification of Al_2O_3/ZrO_2 laminates fabricated by tape casting and sintering. Several kinds of damage or crack occurred during the process including channeling in the tensile layer, edge effect cracks, delamination or interface cracking, and cracks parallel to the interface in the compressive layer. An investigation in room and high temperature failure mechanisms in SOFC electrolytes was carried out by Lowrie and Rawlings [15]. They found that for 8 mol% yttria-stabilized zirconia (YSZ), the room temperature flexure failure test was dependant on surface flaws with fracture initiating at porous defects. At higher temperatures, however, crack initiation and propagation mechanisms changed and fracture also occurred at featureless areas. Overall, the increase in temperature caused a 23–30% reduction in flexural strength. Experiments on ceramic layers (Ni/YSZ–YSZ–$LaMnO_3$) under thermal shock loading revealed that the dominant failure modes to be transgranular fracture at locations of high thermal gradients and inter-granular at high temperature regions. Spalling failure of SOFC components was due to cracking normal to the planes, but interfacial cracking was also present [16]. The fracture toughness and stable crack growth behavior of the treated YSZ was investigated and was compared with that of pure YSZ by Kumar and Sorensen [17]. The crack mode for all the surface treated ceramics was found to be principally transgranular. Studies on

* Corresponding author at: 2034 Black Engineering Building, Iowa State University, Ames, IA 50011, USA. Tel.: +1 515 294 6938; fax: +1 515 294 3261.
E-mail address: gykim@iastate.edu (G.-Y. Kim).

0378-7753/$ – see front matter © 2009 Elsevier B.V. All rights reserved.
doi:10.1016/j.jpowsour.2009.10.064

Nomenclature

a	material constant.
b	the average spacing between microscale damage.
D	the average size of microscale damage.
E_1, E_2	Young's moduli for materials of bonded layers.
E_a	Young's modulus for materials of bonded layers.
E_i'	the plane strain modulus.
G_a	shear modulus of interfacial layer.
h_1,	thickness of top layer.
h_2	thickness of bottom layer.
h_a	thickness of interfacial layer.
K	stress intensity factor.
K_I	opening stress intensity factor.
K_{II}	in plane shear stress intensity factor.
l_1, l_2	half length of top and bottom layers.
n	material constant.
N	the number of thermal cycle.
$N_{nucleation}$	the maximum number of thermal cycling the material sustain before a macroscopic crack appears.
p	porosity of electrode.
u	additional cyclic sliding.
v	additional cyclic stretching.
ν_1, ν_2,	Poisson's ratio of top and bottom layer.
ν_a,	Poisson's ratio of interfacial layer.
α_1, α_2	coefficient of thermal expansion for materials of bonded layers.
β	material constant.
Δ	value variation.
ΔK_I	mode I cyclic stress intensity factor at a microcrack tip.
ΔK_{II}	mode II cyclic stress intensity factor at a microcrack tip
ζ	calculation parameter.
δ_{open}	crack opening displacement.
δ_{shear}	crack sliding displacement.
$\Delta\sigma$	amplitude of local cyclic normal stresses.
$\Delta\tau$	amplitude of local cyclic shear stresses.
λ	the ratio of damage cluster size to average microcrack spacing.
ξ	calculation parameter.
σ	peeling stress.
$\sigma_{thermal}$	interfacial stress at the free edge ($x = l_1$).
$\sigma_{peeling}$	interfacial peeling stress.
$\tau_{interfacial}$	interfacial shear stress.
χ	calculation parameter.
ω	non-dimensional damage parameter.
$\omega_{average}$	the average damage level in the localized damage region of interfacial layer.
ω_{max}	the maximum damage level in the localized damage region of interfacial layer.
"′"	normalized parameter.

production techniques found lower strengths for electrolyte–anode layers when sintered at higher temperatures due to higher interfacial fracture toughness deflecting cracking through the layers [18].

Cycling of SOFCs can cause thermomechanical degradation in material integrity and in performance, which increases rapidly with redox cycles and especially with thermal cycles. Sarantaridis et al. [12] investigated oxidation failure modes of nickel-based anode-supported SOFCs aiming at understanding how much oxidation such a cell can tolerate before catastrophic mechanical failure happens. Faes et al. [13] carried on redox study of anode-supported SOFCs. They applied two techniques to quantify the anode expansion after a redox cycle of nickel at different temperatures. Both of Sarantaridis and Fase experiments showed the cracking of electrolyte after the cycling of SOFCs. As to the thermal cycling performance of SOFC, Bujalski et al. [5] studied the transient performance of three types of SOFCs under different thermal cycling conditions in order to understand the degradation mechanisms. Taniguchi et al. [19] have investigated electrolyte-supported planar SOFC. They found the electrolyte cracked in the area contacting glass sealing materials after one thermal cycle. The thermal cycling performance can be improved by modifying sealing materials and configuration. Hart et al. [20] investigated the thermal cycling of SOFC fabricated by screen printing. It was found that thermal cycling performance degraded greatly during the fifth cycle while the open circuit voltage (OCV) was not reduced significantly during the whole 10 cycles. Tang et al. [21] have investigated the thermal cycling performance of an anode-supported cell between 200 and 750 °C and reached 50 thermal cycles with average OCV loss of 1 mV cycle^{-1}. Schiller et al. [22] reported the results of thermal cycling performance of a metal supported SOFC. The electrode polarization resistance increased and OCV decreased, which was cycled between 180 and 800 °C for 10 thermal cycles. They concluded that the resistance increase indicated some minor electrode delamination and the drop of OCV could be due to the leakage as a result of crack formation in the electrolyte or at seals. Ivers-Tiffée et al. [10] found that SOFC degradation caused by thermal cycling was mainly due to the electrode delamination. The delamination may happen after only several thermal cycles under specific operation conditions. Since the real delamination area was difficult to measure during thermal cycling, finite element (FE) and numerical analysis approaches have been used to estimate the area of delamination in SOFC. However, FE analysis requires a pre-existing crack tip or initial interfacial flaw in SOFC structure [10,13,23,24] and is usually confined to a specific configuration.

Currently, much attention has been focused on the analysis of SOFC performance under thermal cycling conditions. Much of the existing work, however, relied on finite element-based approach rather than modeling from first principles of delamination in layered structures. There have been very few thermomechanical modeling techniques that can be used to assess the reliability and durability of different configurations of SOFC. A fundamental theory-based numerical model is better suited for incorporation within a design and lifetime cycle prediction framework. In this paper, a multi-scale micromechanics model [25] capable of calculating thermal stresses and predicting crack nucleation has been developed. The model integrates thermal stress calculation into crack nucleation model to predict the SOFC lifetime. The model is capable of providing stress distribution and crack nucleation under thermal cycling conditions. This thermomechanical model is generalized and utilized for the lifetime prediction of SOFCs with different configurations.

2. Thermomechanical modeling

A SOFC consists of an anode, electrolyte, and cathode. Amongst SOFCs, most widely used electrolyte is the YSZ ceramic, which exhibits high ionic conductivity, good thermal and chemical stability, and great mechanical strength at high temperatures [26–28]. Commonly, the anode is made of nickel yttria-stabilized zirconia composites (Ni/8YSZ) and is usually 20–40% porous, which displays excellent catalytic properties for fuel oxidation and good current collection capability [29,30]. Because Sr-doped lanthanum manganate ($La_{0.75}Sr_{0.2}MnO_3$) has high electronic conductivity and is also effective catalyst for the dissociation of O_2, it has also been frequently used as cathode [31,32]. This study considers two

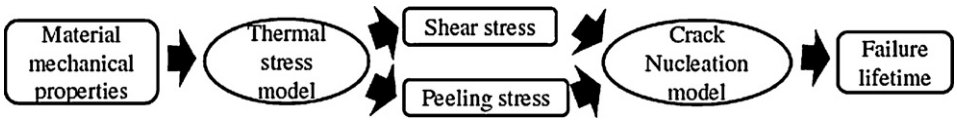

Fig. 1. Schematic of the concept of modeling approach.

variations of SOFC configuration: electrolyte-supported and anode-supported. Electrolyte-supported SOFC operates around 1000 °C. The thickness of an electrode is about 50 μm and that of electrolyte is thicker than 100 μm. In the anode-supported configuration, the electrolyte is usually very thin (less than 20 μm), and cathode is thicker than the electrolyte but much thinner than the anode (50 μm). The thickness of anode varies between 0.3 and 1.5 mm. Since the operating temperature is mainly determined by the nature of the electrolyte, such as the thickness of the electrolyte and its ionic conductivity [33], it can be lowered if the electrolyte becomes thin or has better ionic conductivity. Compared with electrolyte-supported SOFC with a much thicker electrolyte, an anode-supported SOFC operates at lower operating temperatures, typically 700–800 °C. Due to the thinner electrolyte thickness anode-supported SOFCs exhibit high electrochemical performance even at reduced temperatures with substantially lower ohmic resistance of the electrolyte [4,34,35].

The thermomechanical model consists of two parts: thermal stress calculation and crack nucleation, which is shown in Fig. 1. The two thermal stresses, interfacial shear stress and peeling stress, are calculated from the mismatch of material mechanical properties of the cell layers. By applying the thermal stresses and using the Paris law [36], the crack damage rate in a localized damaged area in the interfacial layer can be obtained. Then, the crack nucleation can be predicted from the crack damage rate and the initial damage distribution in the interfacial layer under the thermal cycling condition.

2.1. Modeling of interfacial shear stress and peeling stress

Many studies [37–40] show that an interfacial zone or layer exists between the electrolyte and electrode because of chemical reactions and diffusion under thermal and redox cycling. This interfacial zone or layer contains the electrochemically active sites and is vulnerable to microstructure changes during cell operation.

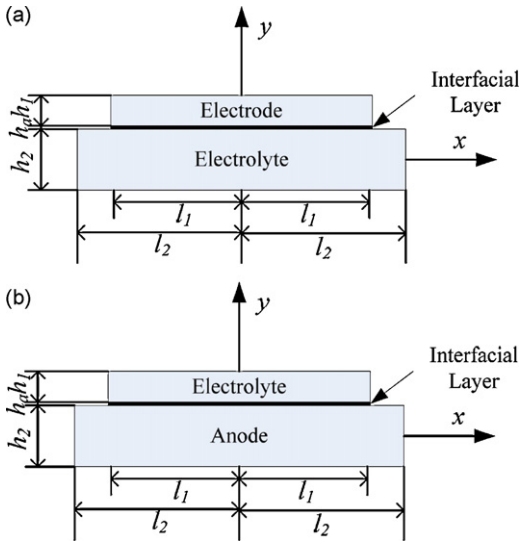

Fig. 2. Schematic of different SOFC configuration (a) Electrolyte-supported (b) Anode-supported.

Therefore, a hypothetical interfacial layer was assumed between the electrodes and the electrolyte, as shown in Fig. 2, where $h_a \ll h_1$ and h_2. The cell is subject to thermal cycling from room temperature to operating temperature, ΔT. Thermal cycling exits in the SOFCs operation, e.g., due to maintenance, fuel supply interruption, or shut-down and restart of plant or device. Also, thermal cycling has been used as a method to investigate SOFC performance degradation and reliability of SOFC structure. A plane strain deformation was assumed in the analysis. Prior research [14–18] suggested that the delamination and transgranular fracture are the two types of SOFC failure. Interfacial shear stress (τ) causes different adjacent layers to detach from each other in parallel direction, and peeling stress leads to different adjacent layers to detach in vertical direction (see Fig. 3). These two types of thermal stresses in a multilayered structure lead to such failures seen in SOFCs. Based on the traction-free boundary condition at the free edge, the interfacial shear stress (τ) and the peeling stress (σ) near a free edge can be expressed as [25,41]:

$$\tau_{interface} = \sigma_{thermal} \exp(-\xi x) \tag{1}$$

where

$$\sigma_{thermal} = \frac{G_a}{h_a \xi}[(1+\nu_1)\alpha_1 - (1+\nu_2)\alpha_2]\Delta T \tag{2}$$

G_a is the shear modulus of the interfacial layer, and is expressed in the following form:

$$G_a = \frac{E_a}{[2(1+\nu_a)]E} \tag{3}$$

Parameter ξ is given by

$$\xi = 2\sqrt{\frac{G_a}{h_a}\left(\frac{1}{E_1' h_1} + \frac{1}{E_2' h_2}\right)} \tag{4}$$

E_i' is the plane strain modulus, given by

$$E_i' = \frac{E_i}{1-\nu_i^2}, \quad i = 1, 2 \tag{5}$$

The peeling stress developed by Jiang et al. [42] is obtained as,

$$\sigma_{peeling} = \zeta \sigma_{thermal} \sigma_0(x) \tag{6}$$

where

$$\sigma_0(x) = \exp(-\xi x) + \exp(-\chi x)$$

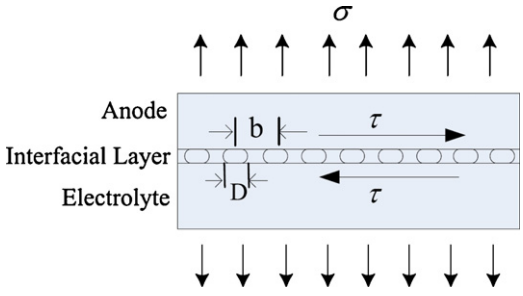

Fig. 3. Schematic diagram of half-SOFC structure with an isothermal and porous homogenous interfacial layer.

$$\times \left(\frac{\xi^2}{2\chi^2} \sin(\chi x) - \left(\frac{\xi^2}{2\chi^2} + \frac{2\chi}{\xi} \right) \cos(\chi x) \right) \quad (7)$$

Parameter χ and ζ are given by,

$$\chi = \left[3\frac{E'_a}{h_a} \left(\frac{1}{E'_1 h_1^3} + \frac{1}{E'_2 h_2^3} \right) \right]^{1/4} \quad (8)$$

$$\zeta = \frac{3(1/E'_1 h_1^2 - 1/E'_2 h_2^2)(h_a/G_a)\xi}{4(1-\nu_a)(1/E'_1 h_1 + 1/E'_2 h_2)^2 + 6(1/E'_1 h_1^3 + 1/E'_2 h_2^3)(h_a/G_a)} \quad (9)$$

2.2. Modeling of crack nucleation

When a multi-layer structure is subjected to thermal cycling, the fracture begins with nucleation of micro-defects, which are followed by propagation of micro-cracks. Eventually, it will lead to the fracture of the multi-layer structure.

The model developed by Huang et al. [43] is generalized and applied to the SOFC structure shown in Fig. 3. During the cyclic loading, a simple form of the kinetic equation can be taken from Paris' law [36],

$$\frac{dD}{dN} = C\left(\frac{\Delta K}{E'_a} \right)^n \quad (10)$$

D is the micro-crack size, C and n are material constants; N is the number of cycles. To simplify the calculation and analysis, ω is introduced as a non-dimensional damage parameter:

$$\omega = \frac{D}{b} \quad (11)$$

b is the micro-crack spacing (see Fig. 3). If $\omega = 0$, no damage is present. When $\omega = 1$, the micro-crack has coalesced into a larger traction-free crack and is considered as nucleation of a macroscopic crack. Therefore, for each loading cycle, the stress intensity factor changes,

$$\Delta K = \Delta\sigma \sqrt{2b \tan \frac{\pi D}{2b}} = \Delta\sigma \sqrt{2b \tan \frac{\pi}{2}\omega} \quad (12)$$

ΔK_I and ΔK_{II} are the different mode stress intensity factors. (ΔK_I means opening stress intensity factor variation (mode I) and ΔK_{II} means in plane shear stress intensity factor variation (mode II).) For the periodic thermal cycle, the cycle stress intensity factors are given by [44].

$$\Delta K_I = \Delta\sigma \sqrt{2b \tan \frac{\pi}{2}\omega} \quad (13)$$

$$\Delta K_{II} = \Delta\tau \sqrt{2b \tan \frac{\pi}{2}\omega} \quad (14)$$

$\Delta\sigma$ and $\Delta\tau$ are the amplitudes of local cyclic normal and shear stresses, respectively. The fatigue growth rate described by Paris' law is expressed below, where β and n are material constants.

$$\frac{dD}{dN} = \beta\left(\sqrt{\Delta K_I^2 + \Delta K_{II}^2} \right)^n \quad (15)$$

Because of the opening and sliding of micro-crack shown in Fig. 3, there will be additional stretch v and additional sliding u across the localized damage band, which can be obtained by averaging the crack opening and crack sliding displacements in damaged layer,

$$v = \frac{1}{b} \int_{-D/2}^{D/2} \delta_{open} dx \quad (16)$$

$$u = \frac{1}{b} \int_{-D/2}^{D/2} \delta_{shear} dx \quad (17)$$

The crack opening and crack sliding displacement can be analyzed by using a configuration of periodical cracks described by Tada et al. [44]

$$\delta_{open} = \frac{4\sigma b}{\pi E'} \cosh^{-1} \frac{\cos(\pi x/b)}{\cos(\pi x/2b)} \quad \text{for } |x| \le \frac{D}{2} \quad (18)$$

$$\delta_{shear} = \frac{4\tau b}{\pi E'} \cosh^{-1} \frac{\cos(\pi x/b)}{\cos(\pi x/2b)} \quad \text{for } |x| \le \frac{D}{2} \quad (19)$$

Additional cyclic stretching Δv and additional cyclic sliding Δu will generate because of the opening and sliding of the micro-cracks in the interfacial layer. The additional cyclic stretching Δv and additional cyclic sliding Δu can be obtained by substituting Eqs. (18) and (19) into Eqs. (16) and (17), respectively.

$$\Delta v = \left(\frac{4}{\pi} \right) \left(\frac{1-\nu_a^2}{E_a} \right) b\Delta\sigma \ln \left(\frac{1}{\cos(\pi D/2b)} \right) \quad (20)$$

$$\Delta u = \left(\frac{4}{\pi} \right) \left(\frac{1-\nu_a^2}{E_a} \right) b\Delta\tau \ln \left(\frac{1}{\cos(\pi D/2b)} \right) \quad (21)$$

Chandra et al. [25] developed a model in which the localized band containing micro-cracks are modeled as an array of dislocation. Therefore, local normal stress $\Delta\sigma$ and local shear stress $\Delta\tau$ can be expressed as

$$\Delta\sigma(x) = \Delta\sigma_{peeling} - \frac{E_a}{4\pi(1-\nu_a^2)} \int_{-\infty}^{\infty} \frac{\partial \Delta v(\xi)}{\partial \xi} \times \frac{d\xi}{x-\xi} \quad (22)$$

$$\Delta\tau(x) = \Delta\tau_{interface} - \frac{E_a}{4\pi(1-\nu_a^2)} \int_{-\infty}^{\infty} \frac{\partial \Delta u(\xi)}{\partial \xi} \times \frac{d\xi}{x-\xi} \quad (23)$$

Normalizing the variables in those equations above, the following non-dimensional parameters are obtained [25]:

$$\sigma' = \frac{\Delta\sigma}{\sigma_{thermal}}, \quad \tau' = \frac{\Delta\tau}{\sigma_{thermal}}, \quad x' = \frac{x}{b}$$

$$v' = \frac{\Delta v}{(b\sigma_{thermal}(1-\nu_a^2))/E_a}, \quad u' = \frac{\Delta u}{(b\sigma_{thermal}(1-\nu_a^2))/E_a} \quad (24)$$

Then, Eqs. (20)–(23) can be rewritten as:

$$v' = \frac{4}{\pi}\sigma' \ln \frac{1}{\cos((\pi/2)\omega)} \quad (25)$$

$$u' = \frac{4}{\pi}\tau' \ln \frac{1}{\cos((\pi s/2)\omega)} \quad (26)$$

$$\sigma' = \zeta\sigma_0(x) - \frac{1}{4\pi} \int_{-\infty}^{\infty} \frac{\partial v'}{\partial \xi'} \times \frac{d\xi'}{x'-\xi'} \quad (27)$$

$$\tau' = \exp(-\lambda x) - \frac{1}{4\pi} \int_{-\infty}^{\infty} \frac{\partial \Delta u'}{\partial \xi'} \times \frac{d\xi'}{x'-\xi'} \quad (28)$$

Therefore, the damage growth rate obtained from Eq. (15) can be expressed as:

$$\frac{d\omega}{dN'} = \left(\tan \frac{\pi}{2}\omega \right)^{n/2} (\sigma' + \tau')^{n/2} \quad (29)$$

The damage distribution $\omega(x)$ is updated with an increment of cycle $\Delta N'$ for the next cycle number $N' + \Delta N'$.

The critical thermal cycle is denoted by $N_{nucleation}$, which is the maximum number of thermal cycles the material can sustain before a macroscopic crack appears in the interfacial layer. $N_{nucleation}$ depends on the material property, $\sigma_{thermal}$ and the initial damage distribution. Following Ohno and Hutchinson [45] and Chandra [25], the initial distribution of damage is used to represent

Table 1
Material properties and geometries used for model validation.

Layer	Young's modulus (GPa)	Poisson ratio	Thickness (μm)	CTE (×10-6 °C^{-1})	ΔT (°C)	Number of cycle at failure	
						Experiment	Calculated
Case 1 [55]	8	9					
Anode (Ni/8YSZ)	60 [54]	0.3 [48,56]	1000	12.5 [52,53]	750		
Electrolyte (YSZ)	200 [54]	0.31 [48,56]	10	10.8 [52,53]			
Case 2 [4]						9	8
Anode (Ni/8YSZ)	56.8 [49,50]	0.258 [49,50]	1500	12.5 [47]	780		
Electrolyte (YSZ)	190 [48]	0.308 [48]	10	10.8 [46,51]			

As to Case 1, the material property is assumed based on product from Versa Power System Ltd. with 40% porosity anode and 5% porosity electrolyte.

Table 2
Material properties and geometries used for the calculation of thermal stresses and lifetime prediction.

Layer	Young's modulus (GPa)	Poisson ratio	Thickness (μm)	CTE (×10-6 °C^{-1})
Electrolyte-supported SOFC				
Anode (Ni/8YSZ)	220 [54,56]	0.3 [48,56]	10,25,40,	12.5 [52,53]
Electrolyte (YSZ)	205 [54,56]	0.31 [48,56]	250	10.3 [52,53]
Cathode (LSM)	114 [54,56]	0.28 [48,56]	25	12.4 [52,53]
Interfacial layer[a]	213/160	0.3	1	11.4
Anode-supported SOFC				
Anode (Ni/8YSZ)	220 [54,56]	0.3 [48,56]	1000	12.5 [52,53]
Electrolyte (YSZ)	205 [54,56]	0.31[48,56]	10,20,30,	10.3 [52,53]
Cathode (LSM)	114 [54,56]	0.28 [48,56]	25	12.4 [52,53]
Interfacial layer[a]	213/160	0.3	1	11.4

[a] The material properties of interfacial layer are assumed between those of anode of electrolyte.

a cluster of damage in the interfacial layer around the electrode edge.

$$\omega(x) = \omega_{average} + (\omega_{\max} - \omega_{average})\exp\left[-\frac{1}{2}\left(\frac{x}{\lambda b}\right)^2\right] \quad (30)$$

$\omega_{average}$ and ω_{max} are the average and maximum damage level in the band. The damage distribution depends much more greatly on ω_{max} than on λ [25]. Since the anode layer is porous structure, the analysis of SOFC structure life prediction is based on the initial damage parameters $\omega_{average} = 0.1$, $\omega_{max} = 0.6$ (porosity $p = 47\%$), $\omega_{max} = 0.5$ (porosity $p = 32\%$), $\omega_{max} = 0.4$ (porosity $p = 17\%$).

3. Material properties for the cell and validation

The modeling results have been compared with two different experimental cases. Parameters used in the simulation for the two cases are summarized in Table 1. The material properties of different SOFC layer used in the validation were chosen from previous literatures [46–54]. In Case 1 [55], it was assumed that the critical thermal cycle for failure was reached when the redox cycle caused significant cell voltage degradation. The modeling calculated critical thermal cycle $N_{nucleation} = 9$, which was almost the same with the value reported in Waldbillig et al. experiment [55] (8 cycles). In Case 2 [4], the critical thermal cycle for failure was estimated by the dramatically increased specific ohmic resistance. The modeling calculated critical thermal cycle $N_{nucleation} = 8$, which was in agreement with the cycle number (9 cycles) in Laurencin et al experiment [4].

Table 3
Young's modulus of electrode at different porosities.

Porosity	Anode (GPa)		Cathode (GPa)		Interfacial layer (GPa)	
	E_0	E_1	E_0	E_1	E_0	E_1
17%	220	99	114	51	213/160	96/72
32%	220	79	114	40	213/160	76/57
47%	220	30	114	15	213/160	29/22

The material properties of different components of a typical electrolyte-supported or anode-supported SOFC (NiO–8YSZ/YSZ/LSM) are chosen from relevant literatures

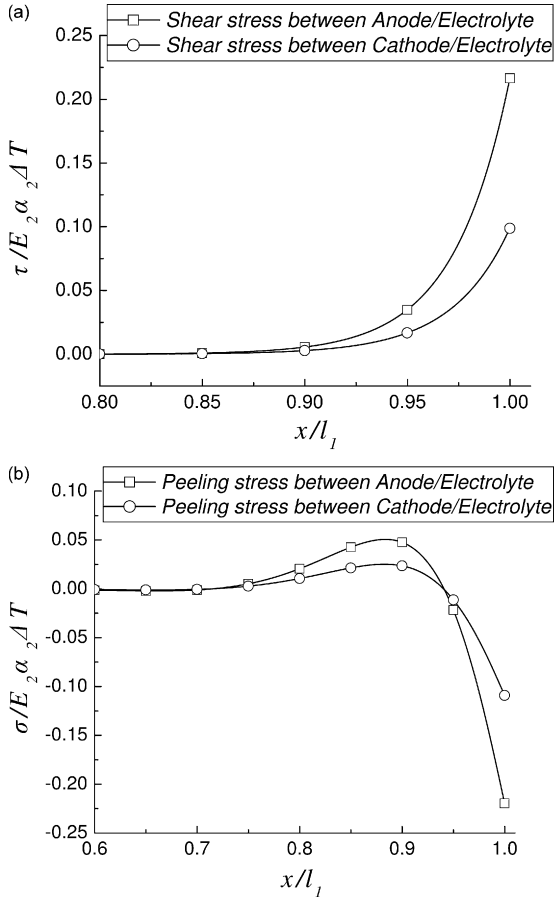

Fig. 4. Thermal stress comparison between anode-electrolyte and cathode-electrolyte in electrolyte-supported SOFC (a) Shear Stress (b) Peeling Stress.

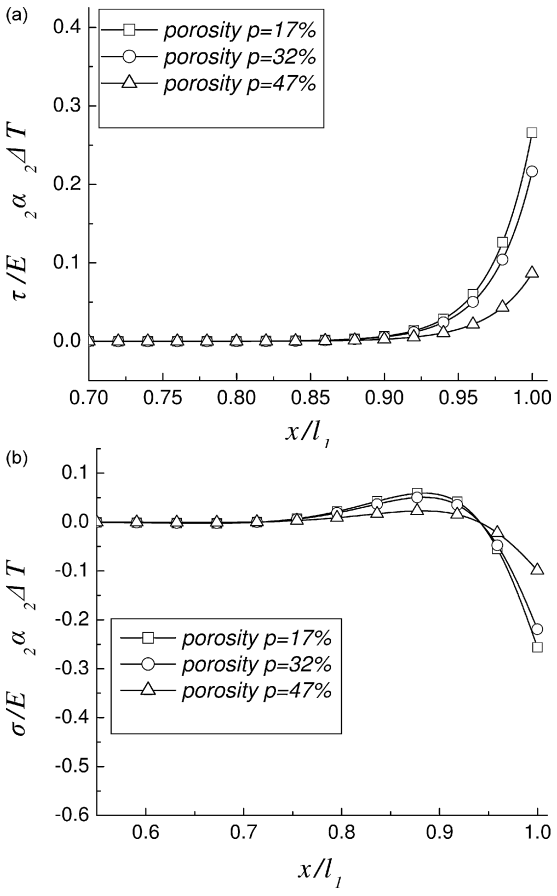

Fig. 5. Thermal stress comparison with different porosity in electrolyte-supported SOFC (a) Shear Stress (b) Peeling Stress.

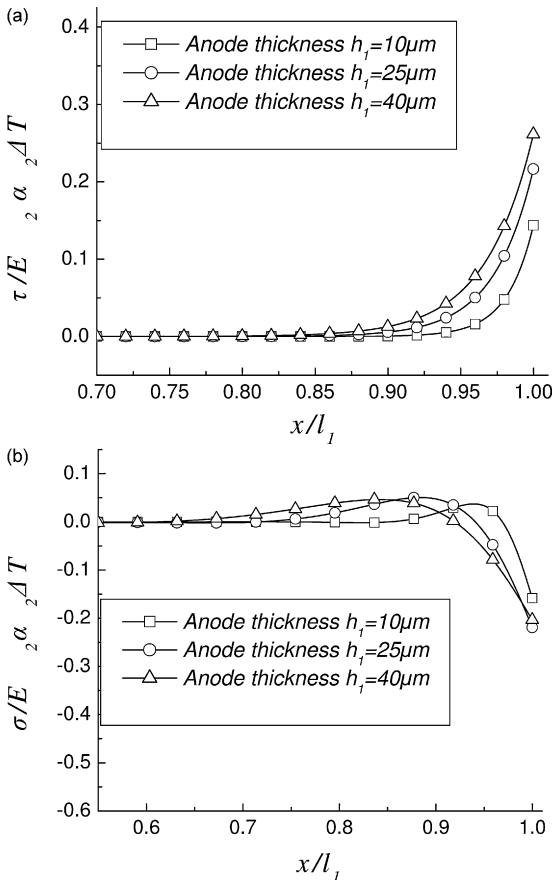

Fig. 7. Thermal stress comparison with different thickness in electrolyte-supported SOFC (a) Shear Stress (b) Peeling Stress.

[48,52–54,56] and are summarized in Table 2. Solid state reaction and inter-diffusion phenomena result in the formation of an interaction zone between the electrodes and the electrolyte under SOFC thermal and redox cycling [40], which forms an interfacial layer reported in [37,39]. The material properties of the interfacial layer are assumed to be between those of the electrode and the electrolyte respectively as shown in Table 2. Based on the interfacial zone or layer thickness in those experiments [37,39,40], the interfacial layer in the modeling calculation is assumed to be 1 μm.

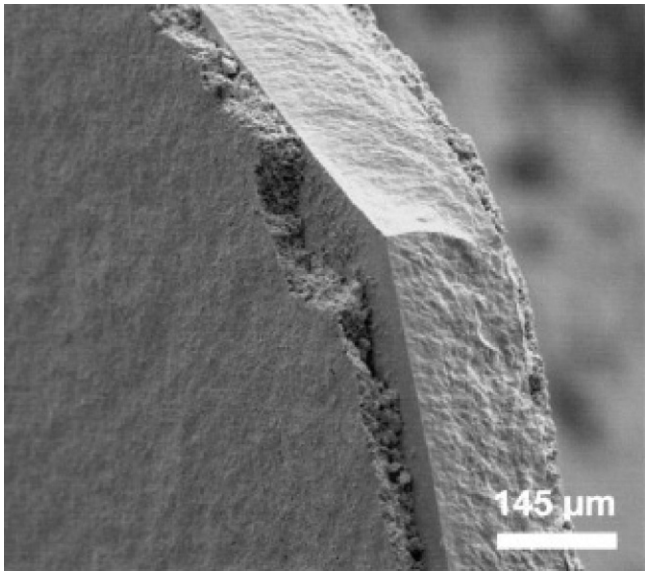

Fig. 6. SEM image of a partially delaminated anode layer on YSZ electrolyte [11].

Since the electrode is a porous structure, its Young's modulus E changes with different porosity. The apparent modulus, E_1 can be calculated as a function of porosity for the same pore structure with semi-empirical correlations. Since the average porosity of anode layer is about 20–40%, three porosities (17%, 32% and 47%) are chosen to analyze the effect of electrode porosity on peeling stress (σ) and interfacial stress (τ). Based on the correlation described in relevant literature [57], the corresponding E_1 with different porosities is summarized and shown in Table 3.

4. Result and discussion

The thermal stresses of anode–electrolyte and cathode–electrolyte interfaces are compared in Fig. 4. The thermal stresses between the anode and electrolyte interface are larger than those between the cathode and electrolyte, and therefore, anode and electrolyte interface is more likely to crack or delaminate under the combined peeling and interfacial shear stresses. This result is in good agreement with other research results reporting delamination susceptibility of the anode–electrolyte interface [2,58,59]. Moreover, the degradation of the anode microstructure mainly determines the overall cell electrical performance [6–9], and therefore, anode–electrolyte was chosen as the focus of this study.

Fig. 5 shows anode porosity effects on interfacial shear and peeling stresses in electrolyte-supported SOFC. With the increase of anode porosity, the interfacial shear stress and peeling stress

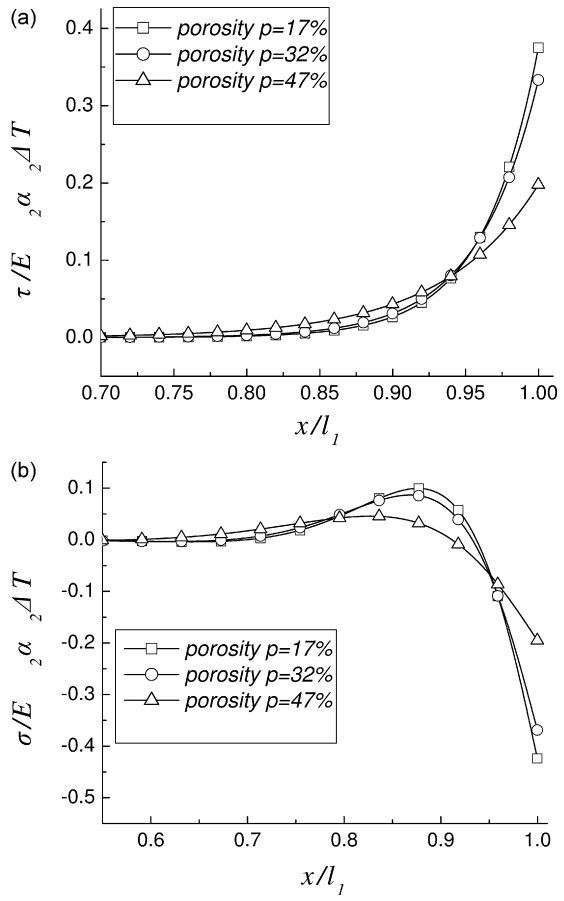

Fig. 8. Thermal stress comparison with different porosity in anode-supported SOFC (a) Shear Stress (b) Peeling Stress.

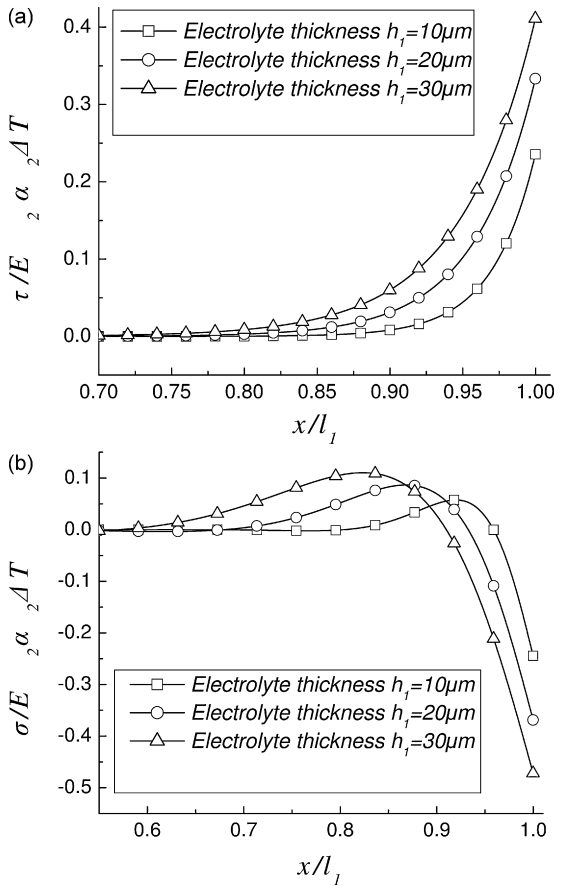

Fig. 9. Thermal stress comparison with different thickness in anode-supported SOFC (a) Shear Stress (b) Peeling Stress.

decrease. When the anode porosity increases from 17% to 47%, the interfacial shear stress almost doubles. The location of peeling stress peak indicates a vulnerable region, which would likely crack or delaminate first. The interfacial shear stress is nearly zero around the center of the specimen and increases sharply towards the edge because of the combined effect of material and geometrical singularities. The peeling stress undergoes severe change from a maximum tensile value to compressive stress near the edge. This trend is similar to layered assemblies under the thermal cycling condition [60]. The combination of these two stresses reaches maximum around the edge of electrode, which is in good agreement with other simulations and measurements made in a similar SOFC configuration. Based on the Weibull approach for failure prediction in a similar SOFC configuration, Laurencin et al. [4,59] predicted that the region around the interfacial area at the edge of electrolyte–electrode will first show signs of damage under thermal cycling. This prediction is confirmed by experimental results by Selcuk et al. [11], which shows a partial delamination of the anode layer edge on the YSZ electrolyte (see Fig. 6).

The effect of anode thickness on interfacial shear and peeling stresses is shown in Fig. 7. With the increase of anode thickness, the thermal stresses increase. For example, if the anode thickness increases from 10 to 40 μm, the interfacial shear stress is almost doubled. Experiment and simulation results performed by Yakabe et al. [35] show that the thermal stresses measured by X-ray diffraction in the cell increases with the increase in anode thickness.

Anode porosity effect on interfacial shear stress and peeling stress in anode-supported SOFC is shown in Fig. 8. The interfacial shear stress and peeling stress have similar trends with those in electrolyte-supported SOFC shown in Fig. 5. The peak value of tensile stress and the amplitude of peeling stress are larger than those in an electrode-supported SOFC (Fig. 9).

Based on the distribution of thermal stresses, the crack nucleation model described in Section 2.2 can predict the damage evolution in the local damage area of the interfacial layer. A typical damage evolution curve is shown in Fig. 10. The propagation of damage accelerates as the cells undergo thermal cycling. The anode-supported SOFC also showed a similar trend.

It can be seen from Fig. 11, the critical thermal cycles for both electrolyte-supported SOFC and anode-supported SOFC decrease with the increase of porosity. Although the increasing porosity of anode reduces the thermal stresses under thermal cycling, it

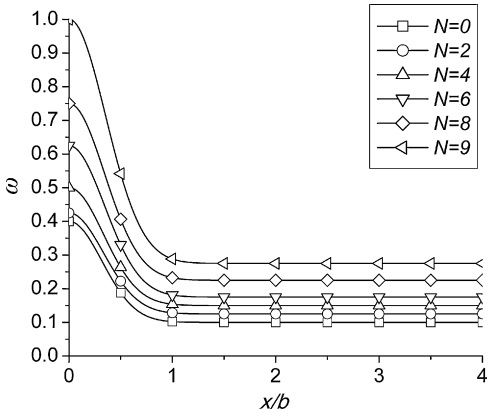

Fig. 10. Damage evolution in electrolyte-supported SOFC (ω_{max} = 0.4 and the anode layer porosity p = 47%).

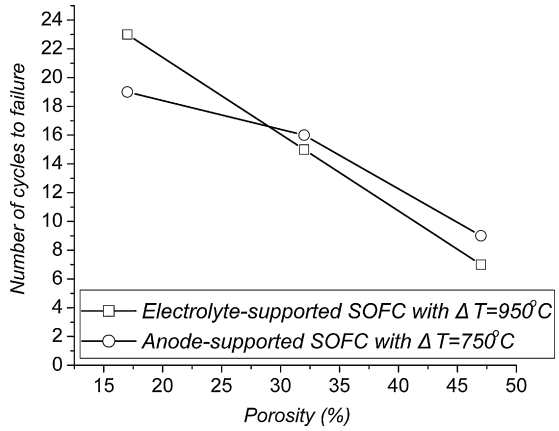

Fig. 11. Anode porosity effect on number of cycles to failure in different SOFC configurations.

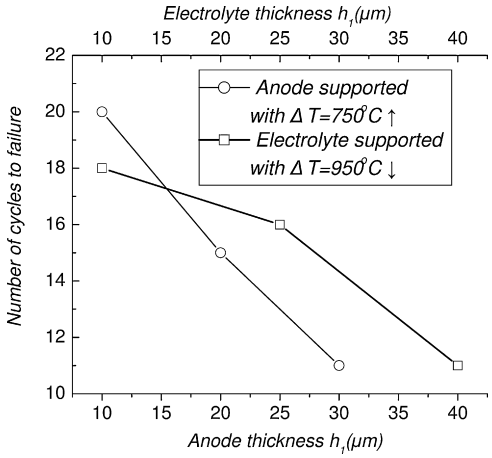

Fig. 12. Anode thickness effect on critical thermal cycle.

increases the initial damage distribution, which also greatly influences the damage evolution. For example, ω_{max} increases from 0.4 to 0.6 with the porosity increasing from 17% to 47%, which has great influence on the critical thermal cycles for failure (see Eq. (30)). That is the reason for the decrease in the thermal cycle numbers to failure with the increase in anode porosity.

The effects of anode thickness variation and electrolyte thickness variation on critical thermal cycle are shown in Fig. 12. It can be clearly concluded that the number of thermal cycles to failure decreases with the increase of anode thickness or electrolyte thickness.

5. Conclusion

A fundamental theory-based numerical model has been proposed and developed to predict the failure of an electrolyte- and anode-supported SOFC under thermal cycling conditions. The modeling approach considered thermal stresses, i.e. interfacial shear stress and peeling stress, arising from the material mismatch between the electrode and electrolyte, and integrated them into the crack propagation model to predict the number of cycles to cell failure. Numerical results were validated against available experimental results, which showed a good agreement. Following conclusion has been drawn from this study.

- The model can effectively provide insight into the evolution and distribution of the thermal stresses during thermal cycling and predict the lifetime of the cell in different configurations.
- The interfacial shear stress and peeling stress were more concentrated near the free edge of SOFCs, which theoretically explains the damage near the cell edges frequently observed in experiments under thermal cycling conditions.
- For the case of nickel-based SOFCs, the anode–electrolyte interface was found to be more prone to delamination under thermal cycling conditions, which explains the high possibility of anode delamination in the electrolyte-supported SOFC in the reported experiments.
- The effects of structural and geometric parameters on the cell lifetime under thermal cycling conditions were investigated. As the porosity and the thickness of anode increased, the lifetime of the cell decreased for the electrolyte-supported cell. A similar trend was found for the anode-supported structure when electrolyte porosity and thickness were varied.

In the future, the model will aid analysis and designing of cell structure for reduced thermal stress and longer cell life, and is expected to contribute towards SOFC reliability and durability research. Currently, integration of degradation mechanisms involving electrochemical pathways such as the influence of the electro-migration on SOFC lifetime is underway. Overall, the model can be used as an effective tool for designing and optimizing the cell structure. A similar modeling framework as described in this study can be applied to analyze the interface reliability in other components of the cell stack that has multi-layered structure.

Acknowledgments

The authors gratefully acknowledge the financial support provided under grant no. CMMI-0640826 of the U.S. National Science Foundation.

References

[1] H. Yokokawa, H. Tu, B. Iwanschitz, A. Mai, J. Power Sources 182 (2008) 400–412.
[2] Y.C. Hsiao, Selman, J. Robert, Solid State Ionics 98 (1997) 33–38.
[3] T. Komatsu, K. Watanabe, M. Arakawa, H. Arai, J. Power Sources 193 (2009) 585–588.
[4] J. Laurencin, G. Delette, B. Morel, F. Lefebvre-Joud, M. Dupeux, J. Power Sources 192 (2009) 344–352.
[5] W. Bujalski, Dikwal, M. Chinnan, Kendall, Kevin, J. Power Sources 171 (2007) 96–100.
[6] T. Fukui, S. Ohara, M. Naito, K. Nogi, Performance and Stability of SOFC Anode Fabricated from NiO/YSZ Composite Particles, Oviedo, Spain, 2002.
[7] A. Hagen, R. Barfod, P.V. Hendriksen, Y.L. Liu, S. Ramousse, J. Electrochem. Soc. 153 (2006) A1165–A1171.
[8] S. Koch, P.V. Hendriksen, M. Mogensen, Y. Liu, N. Dekker, B. Rietveld, B. de Haart, F. Tietz, Solid Oxide Fuel Cell Performance Under Severe Operating Conditions, Luzerne, Switzerland, 2006.
[9] J.H. Lee, J.W. Heo, D.S. Lee, J. Kim, G.H. Kim, H.W. Lee, H.S. Song, J.H. Moon, Solid State Ionics 158 (2003) 225–232.
[10] D. Herbstritt, A. Krugel, A. Weber, E. Ivers-Tiffee, Thermocyclic Load: Delamination Defects and Electrical Performance of Single Cells, Tsukuba, Japan, 2001.
[11] A. Selcuk, G. Merere, A. Atkinson, J. Mater. Sci. 36 (2001) 1173–1182.
[12] D. Sarantaridis, R.A. Rudkin, A. Atkinson, J. Power Sources 180 (2008) 704–710.
[13] A. Faes, A. Nakajo, A. Hessler-Wyser, D. Dubois, A. Brisse, S. Modena, J. Van herle, J. Power Sources 193 (2009) 55–64.
[14] P.Z. Cai, D.J. Green, G.L. Messing, J. Am. Ceram. Soc. 80 (1997) 1929–1939.
[15] F.L. Lowrie, R.D. Rawlings, J. Eur. Ceram. Soc. 20 (2000) 751–760.
[16] E.P. Busso, Y. Tkach, R.P. Travis, Philos. Mag. A—Phys./Condens. Matter Struct. Defects Mech. Prop. 81 (2001) 1979–1995.
[17] A.N. Kumar, B.F. Sorensen, Mater. Sci. Eng. Prop. Microstruct. Process. 333 (2002) 380–389.
[18] B.F. Sorensen, S. Primdahl, J. Mater. Sci. 33 (1998) 5291–5300.
[19] S. Taniguchi, M. Kadowaki, T. Yasuo, Y. Akiyama, Y. Miyake, K. Nishio, J. Power Sources 90 (2000) 163–169.
[20] N.T. Hart, Scale-up of the IP-SOFC to multi kilowatt levels, DTI/F/01/00197/REP URN 04/556 (2004).
[21] D.P.E. Tang, M. Pastula, B. Borglum, in: S.C. Singhal, J. Mizusaki (Eds.), SOFC IX, Pennington, NJ, 2005.
[22] G. Schiller, T. Franco, M. Lang, P. Metzger, and A. Störmer, Recent Results on the SOFC APU Development at DLR, Proc. Electrochemical Society, Vol. 2005-07, p 66-75, Internat. Symp. On Solid Oxide Fuel Cells (SOFC-IX), May 2005.(Quebec City, Canada).

[23] X. Sun, W.N. Liu, E. Stephens, M.A. Khaleel, J. Power Sources 176 (2008) 167–174.
[24] S. Pitakthapanaphong, E.P. Busso, Modell. Simul. Mater. Sci. Eng. 13 (2005) 531–540.
[25] A. Chandra, Y. Huang, Z.Q. Jiang, K.X. Hu, G. Fu, J. Electron. Packag. 122 (2000) 220–226.
[26] C. Yang, W. Li, S. Zhang, L. Bi, R. Peng, C. Chen, W. Liu, J. Power Sources 187 (2009) 90–92.
[27] C. Brahim, A. Ringued, E. Gourba, M. Cassir, A. Billard, P. Briois, J. Power Sources 156 (2006) 45–49.
[28] M. Han, X. Tang, H. Yin, S. Peng, J. Power Sources 165 (2007) 757–763.
[29] J.H. Yu, G.W. Park, S. Lee, S.K. Woo, J. Power Sources 163 (2007) 926–932.
[30] V.A.C. Haanappel, J. Mertens, J. Malzbender, J. Power Sources 171 (2007) 789–792.
[31] X. Li, Principles of Fuel Cells, Taylor & Francis Group, New York, 2006.
[32] P. Leone, M. Santarelli, P. Asinari, M. Cal, R. Borchiellini, J. Power Sources 177 (2008) 111–122.
[33] R.M. Ormerod, Chem. Soc. Rev. 32 (2003) 17–28.
[34] B. Zhonghe, Y. Baolian, W. Zhenwei, D. Yonglai, W. Hejin, S. Yunchuan, C. Mojie, Electrochem. Solid-State Lett. 7 (2004) A105–A107.
[35] H. Yakabe, Y. Baba, T. Sakurai, Y. Yoshitaka, J. Power Sources 135 (2004) 9–16.
[36] T.L. Anderson, Fracture Mechanics Fundamental and Applications, Taylor & Francis Group, New York, 2005.
[37] X. Zhang, S. Ohara, R. Maric, H. Okawa, T. Fukui, H. Yoshida, T. Inagaki, K. Miura, Solid State Ionics 133 (2000) 153–160.
[38] N. Maffei, G. de Silveira, Solid State Ionics 159 (2003) 209–216.
[39] Y.L. Liu, C.G. Jiao, Solid State Ionics 176 (2005) 435–442.
[40] A. Tsoga, A. Gupta, A. Naoumidis, P. Nikolopoulos, Acta Mater. 48 (2000) 4709–4714.
[41] K.P. Wang, Y.Y. Huang, A. Chandra, K.X. Hu, IEEE Trans. Compon. Packag. Technol. 23 (2000) 309–316.
[42] Z.Q. Jiang, Y. Huang, A. Chandra, J. Electron. Packag. 119 (1997) 127–132.
[43] Y. Huang, X.Y. Gong, Z. Suo, Z.Q. Jiang, Int. J. Solids Struct. 34 (1997) 3941–3951.
[44] P.P.H. Tada, G.R. Irwin, The Stress Analysis of Cracks Handbook, Del. Research, St. Louis, 1985.
[45] N. Ohno, J.W. Hutchinson, J. Mech. Phys. Solids 32 (1984) 63–85.
[46] S.T. Aruna, M. Muthuraman, K.C. Patil, Solid State Ionics 111 (1998) 45–51.
[47] F. Tietz, Ionics 5 (1999) 129–139.
[48] A. Atkinson, A. Selcuk, Solid State Ionics 134 (2000) 59–66.
[49] R. Miladin, L.C. Edgar, J. Am. Ceram. Soc. 87 (2004) 2242–2246.
[50] R. Miladin, L.C. Edgar, Acta Mater. 52 (2004) 5747–5756.
[51] A. Nakajo, C. Stiller, G. Härkegård, O. Bolland, J. Power Sources 158 (2006) 287–294.
[52] M. Mori, T. Yamamoto, H. Itoh, H. Inaba, H. Tagawa, J. Electrochem. Soc. 145 (1998) 1374–1381.
[53] S. Sameshima, T. Ichikawa, M. Kawaminami, Y. Hirata, Mater. Chem. Phys. 61 (1999) 31–35.
[54] M. Pihlatie, A. Kaiser, M. Mogensen, Mechanical properties of NiO/Ni–YSZ composites depending on temperature, porosity and redox cycling, J, Eur. Ceram. Soc. 29 (2009) 1657–1664.
[55] D. Waldbillig, A. Wood, D.G. Ivey, J. Power Sources 145 (2005) 206–215.
[56] S. Giraud, J. Canel, J. Eur. Ceram. Soc. 28 (2008) 77–83.
[57] J.C. Wang, J. Mater. Sci. 19 (1984) 801–808.
[58] T. Zhang, Q. Zhu, W.L. Huang, Z. Xie, X. Xin, J. Power Sources 182 (2008) 540–545.
[59] J. Laurencin, G. Delette, F. Lefebvre-Joud, A. Dupeux, J. Eur. Ceram. Soc. 28 (2008) 1857–1869.
[60] J.L. Wang, S.X. Zeng, J. Appl. Phys. 104 (2008) 113501–113508.